UNIVERSITYOF BIRMINGHAM

Effects of altered cellular ultrastructure on energy metabolism in diabetic cardiomyopathy

Ghosh, Shouryadipta; Guglielmi, Giovanni; Orfanidis, Ioannis ; Spill, Fabian; Hickey, Anthony; Hanssen, Eric ; Rajagopal, Vijay

Document Version
Publisher's PDF, also known as Version of record

Citation for published version (Harvard):
Ghosh, S, Guglielmi, G, Orfanidis, I, Spill, F, Hickey, A, Hanssen, E & Rajagopal, V 2022, 'Effects of altered cellular ultrastructure on energy metabolism in diabetic cardiomyopathy: an in-silico study', *Royal Society of London. Proceedings B. Biological Sciences*, vol. 377, no. 1864, 20210323.
https://doi.org/10.1098/rstb.2021.0323

[Link to publication on Research at Birmingham portal](#)

THE ROYAL SOCIETY PUBLISHING

Effects of altered cellular ultrastructure on energy metabolism in diabetic cardiomyopathy: an *in silico* study

Shouryadipta Ghosh[1,2], Giovanni Guglielmi[2,4], Ioannis Orfanidis[5], Fabian Spill[4], Anthony Hickey[6], Eric Hanssen[3] and Vijay Rajagopal[2]

[1]CSIRO Data61, Commonwealth Scientific and Industrial Research Organisation, Research Way, Clayton, VIC 3168, Australia
[2]Department of Biomedical Engineering, and [3]Ian Holmes Imaging Center and Department of Biochemistry and Pharmacology, Bio21 Institute, University of Melbourne, Parkville, VIC 3010, Australia
[4]School of Mathematics, University of Birmingham, Edgbaston B15 2TS, UK
[5]Health Data Specialists, Grand Canal Docklands, Dublin D02 VK08, Republic of Ireland
[6]School of Biological Sciences, University of Auckland, Auckland, NZ 1042, New Zealand

SG, 0000-0001-5764-0592; AH, 0000-0003-3784-4816; VR, 0000-0002-5509-402X

Diabetic cardiomyopathy is a leading cause of heart failure in diabetes. At the cellular level, diabetic cardiomyopathy leads to altered mitochondrial energy metabolism and cardiomyocyte ultrastructure. We combined electron microscopy (EM) and computational modelling to understand the impact of diabetes-induced ultrastructural changes on cardiac bioenergetics. We collected transverse micrographs of multiple control and type I diabetic rat cardiomyocytes using EM. Micrographs were converted to finite-element meshes, and bioenergetics was simulated over them using a biophysical model. The simulations also incorporated depressed mitochondrial capacity for oxidative phosphorylation (OXPHOS) and creatine kinase (CK) reactions to simulate diabetes-induced mitochondrial dysfunction. Analysis of micrographs revealed a 14% decline in mitochondrial area fraction in diabetic cardiomyocytes, and an irregular arrangement of mitochondria and myofibrils. Simulations predicted that this irregular arrangement, coupled with the depressed activity of mitochondrial CK enzymes, leads to large spatial variation in adenosine diphosphate (ADP)/adenosine triphosphate (ATP) ratio profile of diabetic cardiomyocytes. However, when spatially averaged, myofibrillar ADP/ATP ratios of a cardiomyocyte do not change with diabetes. Instead, average concentration of inorganic phosphate rises by 40% owing to lower mitochondrial area fraction and dysfunction in OXPHOS. These simulations indicate that a disorganized cellular ultrastructure negatively impacts metabolite transport in diabetic cardiomyopathy.

This article is part of the theme issue 'The cardiomyocyte: new revelations on the interplay between architecture and function in growth, health, and disease'.

1. Introduction

Type I diabetes (T1D) accounts for 5–10% of all diabetes cases every year [1,2]. T1D can lead to a variety of cardiovascular complications eventually resulting in heart failure. T1D cardiomyopathy is one of the T1D-induced disease processes, commonly associated with left ventricular diastolic dysfunction with normal ejection fraction [3]. It exhibits many common metabolic conditions accompanying heart failure, e.g. increased synthesis of reactive oxygen species (ROS) [4,5], impaired mitochondrial oxidative phosphorylation (OXPHOS) [5–7] and decrease in both cellular reserve of phosphocreatine (PCr) and activity of mitochondrial creatine kinase (mtCK) enzymes regulating PCr levels [8,9].

T1D cardiomyopathy is also accompanied by alterations in the ultrastructure of cardiomyocytes. Cardiomyocytes are densely packed with three-dimensional mitochondrial networks [10,11] and columns of myofibrils that traverse parallelly across the length of cells. The mitochondrial networks are formed by close contact between the outer membrane of two adjacent mitochondria [10–13]. In T1D cardiomyopathy, this columnar ultrastructure is altered with changes both in morphology and organization of mitochondria and myofibrils [6,14,15]. Similar changes are also observed in several other pathological conditions of the heart [16–18]. However, the functional role or consequence of these ultrastructural alterations is unclear. In this study, we use T1D cardiomyopathy as a model disease state to understand how and to what extent the accompanying changes in cardiomyocyte ultrastructure can influence cellular energy metabolism.

The majority of previous studies point towards increased mitochondrial fission as the key mechanism underlying the change in mitochondria organization and morphology in T1D cardiomyopathy. Increased mitochondrial fission in T1D cardiomyopathy is characterized by smaller mitochondria with higher numeric density [19–21]. Our recent study on streptozotocin (STZ)-induced T1D in Sprague Dawley (SD) rats further showed that fragmented individual mitochondria cluster together to form mitochondrial clusters of varying shapes and sizes [21]. Several studies also report mitochondrial proliferation in the form of higher mitochondrial volume fraction in T1D cardiomyocytes [6,15,22]. However, these reports conflict with few other studies where mitochondrial content is found to be either unchanged [23] or decreased [24,25] with T1D. A potential reason behind these conflicting results can be the use of small regions of interest (ROI) on electron microscopy (EM) images. EM micrographs of small ROIs provide great insights at a local level but lacks insights on how mitochondrial organization is affected across the cell. In addition to changes in mitochondrial organization, T1D can also disrupt the organization of other organelles such as myofibrils, t-tubules and sarcoplasmic reticulum [24,26].

In our unpublished work on STZ-induced T1D in SD rats, substantial changes in cardiomyocyte ultrastructure were only observed 8–9 weeks after injection of STZ. In another relevant study on Alloxan-induced T1D in SD rats, Thomson et al. [26] observed that only approximately 15% of all cardiomyocytes in the left ventricle undergo structural disorganization after six weeks of diabetes. The percentage of disorganized cardiomyocyte increases up to 60% after 26 weeks. By contrast, four-week post-STZ injection is sufficient to observe significant changes in cardiac mitochondrial metabolism, e.g. decline in mitochondrial state III oxygen consumption [7] and activity of mtCK enzymes [9,27]. Are the subsequent ultrastructural changes adaptive in nature or do they compound the negative consequences of disrupted mitochondrial metabolism?

A previous study by Shen et al. [14] on OVE26 mice suggests mitochondrial proliferation to be an adaptive response to mitochondrial dysfunction such as increased ROS production. However, two other works on insulin-resistant mice indicate that higher mitochondrial volume fraction and DNA content might not be able to compensate for a decrease in respiratory capacity of individual mitochondria [28,29]. In our recent in silico analysis of energy metabolism

in control cardiomyocytes, we found that creatine kinase (CK)-mediated rapid phospho-transfer can maintain near uniform ATP and ADP levels across a cell cross-section, despite a non-uniform arrangement of mitochondrial and myofibrillar columns [30]. Since CK enzyme activity is reported to be substantially lower in T1D cardiomyocytes [9,27], disorganization of organelles might negatively impact the cellular mechano-energetic landscape.

The primary aim of the current study was to investigate how and to what extent various ultrastructural alterations accompanying T1D cardiomyopathy can influence the energy metabolism of cardiomyocytes. We used a combination of EM imaging and in silico modelling that allowed us to decouple the interactions between ultrastructural alterations and alterations in mitochondrial metabolism and examine their cumulative effects on cardiac bioenergetics. We first collected and analysed EM images of entire cross-sections of cardiomyocytes from control and STZ-induced T1D rats. Next, we used our finite-element (FE) model of cardiac bioenergetics [30,31] to simulate both control and diabetic bioenergetics over spatially realistic FE meshes derived from these cross-sectional EM images. The simulation predictions revealed that ultrastructural changes such as lower mitochondrial fraction and irregular mitochondrial arrangement further compound the disruptive effects of preceding metabolic dysfunction such as impaired OXPHOS capacity and lower mtCK enzyme activity. The following sections present the image analysis, formulation of the FE models and the subsequent simulation predictions. Our results support a hypothesis that cardiomyocyte ultrastructural changes found in T1D negatively impact cardiac bioenergetics.

2. Methods

(a) Tissue sample preparation and transmission electron microscopy

The animal procedures in this study followed the guidelines approved by the University of Auckland Animal Ethics Committee (for animal procedures conducted in Auckland, Application No. R826). Six SD rats were randomly distributed into a control and a T1D group and raised in two separate cages. After six weeks, T1D was induced in three six-week-old male SD rats by injecting them with a single dose of STZ (55 mg kg^{-1} body wt) in saline medium. The same volume of saline without STZ was injected into the three control animals of same age. The T1D animals were euthanized nine weeks after the injections, while the control animals were euthanized seven–nine weeks after the injections. Following sacrifice, hearts were excised, and 400–600 μm side cubes of tissue from the ventricular mid-wall of each control and diabetic hearts were chemically fixed (2.5% glutaraldehyde, 2% paraformaldehyde and 50 mM CaCl2 in 0.15 M sodium cacodylate buffer) [32] and processed for standard transmission electron microscopy (TEM). Ultrathin sections of 90 nm thickness were subsequently cut from epoxy resin blocks using a diamond knife and used for TEM imaging.

A Tecnai Spirit TEM operated at 120 kV was used to acquire the majority of the transverse-view two-dimensional micrographs with pixel size varying from 5.6 nm to 13.5 nm. A few sections were also imaged with a smaller pixel size of 2.3 nm using a Tecnai F30 TEM operated at 200 kV. Ultimately, a total of 21 diabetic cardiomyocyte cross-sections and 19 control cardiomyocyte cross-sections (electronic supplementary material, Methods S1) were selected from the collected transverse-view images (a

minimum of five cross-sections per animal). All the cross-section images were acquired away from the cell nucleus [33].

(b) Image segmentation and analysis of cellular ultrastructure

Trainable Weka Segmentation plugin of IMAGEJ [34], an open-source EM image processing software package was used to roughly segment each cell cross-section into four organelle-based regions: (i) mitochondria, (ii) myofibrils, (iii) t-tubules and intracellular vacuoles, and (iv) glycogen particles. The rough segmentations were further manually corrected using selection tools available in IMAGEJ. Figure 1a,b represents final segmentations of two typical cross-sections of control and diabetic cardiomyocytes used in the study. The segmented transverse sections were first analysed for area fractions of the different organelles; e.g. area fraction of mitochondria in each cell cross-section was calculated as a ratio of total number of pixels marked as mitochondria versus total number of pixels within the cell cross-section. This process was repeated for all the four organelle regions (figure 1c). The ratio of mitochondrial area fraction against total mitochondrial and myofibrillar area fraction was defined as mito/myo$_{global}$ of each section.

Following the calculation of area fractions, the distribution of ATP producing sites (mitochondria) with respect to the ATP consuming sites (myofibrils) was analysed for each cell cross-section. In this analysis, a square sampling window of fixed size was assumed to be centred at every pixel marked as myofibril (electronic supplementary material, figure S1A). Each sampling window was analysed for the ratio of total mitochondrial pixels against total mitochondrial and myofibrillar pixels present within the window. This ratio was termed as the localized area density of mitochondria (mito/myo$_{local}$) for a given myofibrillar pixel. The side length of the square sampling window was 1.6 μm—which is twice the average diameter of cardiac mitochondria. A further justification of this choice of sampling window length can be found in our previous work [30]. The electronic supplementary material, figure S1A and B maps the resulting mito/myo$_{local}$ distribution in the representative cross-sections shown in figure 1a,b. The inset in the electronic supplementary material, figure S1C further shows the histogram representation of these two mito/myo$_{local}$ distributions. To quantify the spatial heterogeneity in mitochondrial–myofibrillar arrangement of a given cross-section, median absolute deviation (MAD) of its mito/myo$_{local}$ distribution was calculated. MAD is a robust measure of variability with little sensitivity to the presence of outliers.

(c) Computational modelling of control cardiomyocytes

Our previous publication [31] provides complete mathematical details of the computational model of control cardiomyocytes used in this study, along with the validation of the model predictions with respect to four experimental datasets. The Fortran source code of the model is available at our GitHub repository—https://github.com/CellSMB/cardiac_bioenergetics/tree/V-2.0. The present section provides a brief outline of the model to assist the readers with interpretation of the simulation results. Figure 2 is a schematic diagram of the different state variables and reaction flux terms that are used in this biophysics-based model. The electronic supplementary material, table S1 provides expanded names of the state variables and reaction fluxes used in figure 2.

The computational models were based on the TEM micrographs used in the image analysis. The segmented images were first converted into FE meshes using an open source tool called TRIANGLE [35]. A previously validated model of OXPHOS in isolated mitochondria [36] was simulated at each mitochondrial node, incorporating differential algebraic equations representing

11 reactions with 13 metabolites (figure 2). Key reaction fluxes modelled include: (i) generation of mitochondrial membrane potential and electron transfer through complex I, III and IV; (ii) generation of ATP at F1-F0 ATP synthase; and (iii) exchange of ATP and ADP through the adenine nucleotide translocases (ANT). However, the isolated mitochondrial model lacked the description of reactions occurring in the mitochondrial inter-membrane space (IMS) and subsequent diffusion of metabolites through the mitochondrial outer membrane to myofibrils. Therefore, equations were also introduced at each mitochondrial node to simulate key IMS reactions. These include the synthesis of PCr catalysed by mtCK, as well as, diffusion of ATP, ADP, adenosine monophosphate (AMP), PCr, creatine (Cr) and inorganic phosphate (Pi) (figure 2). The IMS and matrix reactions were modelled as two reaction compartments continuously distributed across the mitochondrial regions. Fluxes of transport reactions such as ANT and phosphate–hydrogen cotransporter mathematically connected both compartments. All reactions fluxes used in the differential equations were scaled by the volume fraction of the respective compartment (VF$_{IMS}$ = 0.1, VF$_{MATRIX}$ = 0.9) to maintain conservation of mass.

Similar to the mitochondrial FE nodes, total five reactions with eight metabolites were modelled in each myofibrillar FE node (figure 2). Out of these metabolites, concentrations of ATP, ADP and Pi were used to calculate the reaction rate of ATP hydrolysis (V_{ATPase}) in each myofibril node (electronic supplementary material, figure S2):

$$V_{ATPase} = \frac{X_{ATPase}}{1 + R_m(Pi*ADP/ATP)},$$

where R_m is a constant of mass-action ratio, while X_{ATPase} is a model input that can be varied to simulate steady state ATP hydrolysis at various workloads. ATP, ADP and Pi were also modelled to diffuse through the myofibrillar nodes towards the mitochondrial nodes. Other key myofibrillar reactions included in the model were regeneration of ATP by myofibrillar CK and buffering of ADP/ATP level by myofibrillar adenylate kinase (AK). The reaction rate of CK in myofibrillar nodes was balanced with that of mtCK in mitochondrial nodes through diffusion of PCr and Cr. Similarly, myofibrillar AK reaction rate was balanced with that of mitochondrial AK through diffusion of AMP. The electronic supplementary material, figure S2 provides the detailed mathematical equation of few key state variables and reaction fluxes for readers to appreciate the biophysical mechanisms modelled through these equations. The values of the diffusion constants of all diffusing species are available in the electronic supplementary material, table S2.

Glycogen particles usually do not contain any enzymes capable of catalysing reactions involving the metabolites such as ATP and ADP. Therefore, no reaction fluxes were calculated in the glycogen FE nodes, although ATP, ADP, PCr, Cr and Pi were assumed to be diffusing through these nodes with the same diffusivities as those of myofibrillar nodes. It was further assumed that none of the metabolites considered in the model are present in the t-tubules and vacuoles. These regions were marked as holes in the FE mesh. The resulting bioenergetics FE model of a TEM micrograph was simulated using OPENCMISS, an opensource FE modelling software [37].

(d) Computational modelling of cardiomyocytes with type I diabetes

As discussed earlier, STZ-induced T1D cardiomyopathy in SD rats is first accompanied by dysfunction in ATP synthesis machinery of mitochondria within four weeks of STZ injection, followed by alterations in intracellular ultrastructure after another 4–5 weeks. Some of the key metabolic changes include:
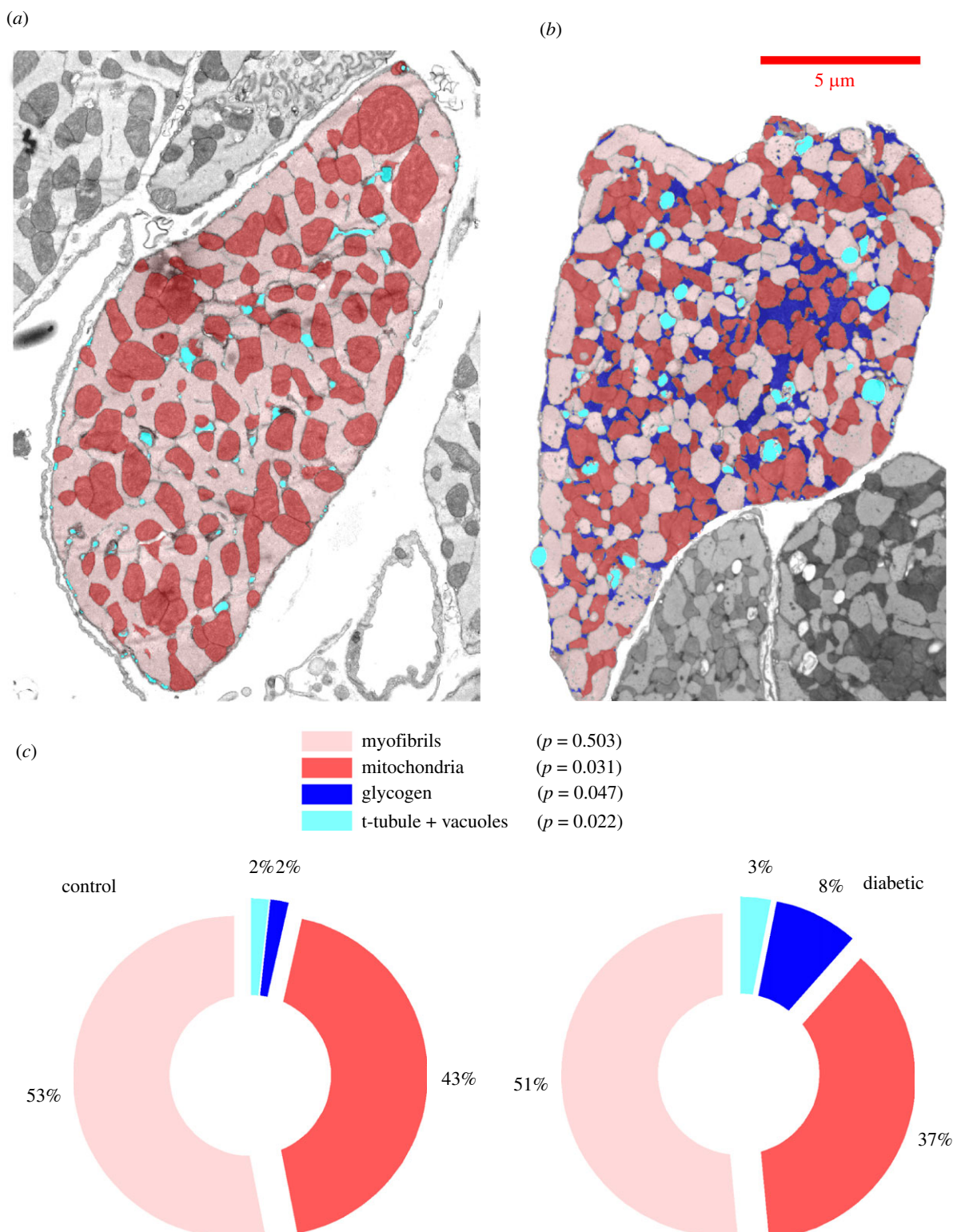
Figure 1. Segmented organelle areas in cardiomyocyte cross-sections and their area fractions. (*a*) Segmentation of organelle areas in a representative cardiomyocyte cross-section from TEM micrograph of a control animal. Segmentations are overlaid over original transverse micrograph. (*b*) Segmentation of organelle areas in a representative cross-section from a diabetic animal. (*c*) Pie charts showing average organelle area fractions in the control and diabetic group. Both groups consist of $n = 3$ animals, with at least five cross-sections analysed for each animal. The *p*-values correspond to the null hypothesis that organelle fractions do not change in diabetes.

(i) decrease in enzymatic activity of several mitochondrial complexes, including complex I [7,23] and F1-F0 ATP synthase [38,39], as well as, mtCK present in IMS [9,27,40]; (ii) elevated level of mitochondrial uncoupling and proton leak [41,42]; and finally (iii), decrease in the level of mitochondrial ATP synthesis [6,7,23], membrane potential [43,44] and O_2 consumption [42,45]. To understand how ultrastructural alterations interplay with mitochondrial dysfunction, diabetic cardiomyocytes were

simulated in two steps. First, diabetic mitochondrial dysfunction was simulated with control cellular ultrastructure (Set CD). Simulations set CD consisted of total 19 simulations based on the 19 control cross-sections used for image analysis. Next, diabetic mitochondrial dysfunction was also simulated with FE meshes derived from diabetic TEM images (Set DD). Set DD consisted of total 21 simulations. Results from both simulations set CD and DD were compared with those derived from simulations
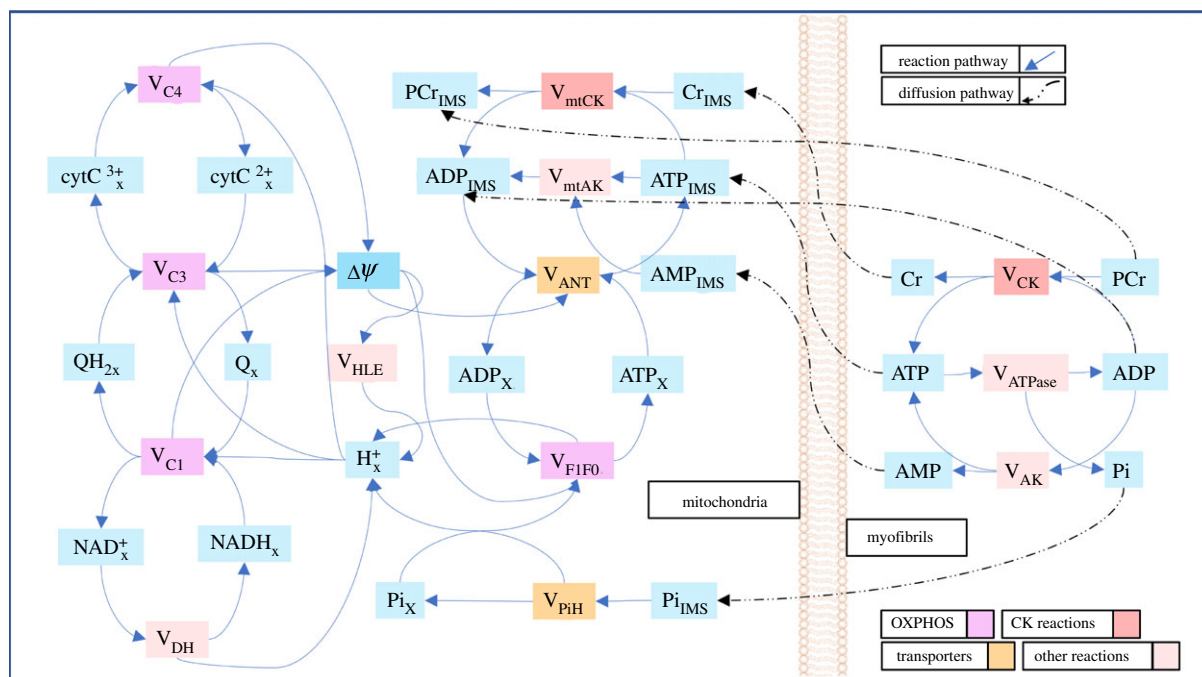
Figure 2. Schematic diagram of the biophysical model of cardiac bioenergetics. The rectangular boxes coloured in cyan represent the state variables of the model. The state variables are molar concentrations of different metabolites present in myofibrils, mitochondrial IMS (suffix - $_{IMS}$) and mitochondrial matrix (suffix - $_\chi$), except for ψ which is mitochondrial membrane potential. All other boxes in the figure represent reaction fluxes involving the state variables. Metabolites present in the myofibrils and mitochondrial IMS also partake in diffusive fluxes across the mitochondria–myofibril interface. The electronic supplementary material, table S1 provides expanded names of the state variables and reaction fluxes used in this figure.

Table 1. Control and diabetic values of key OXPHOS parameters altered in the mitochondrial energy metabolism model.

parameter	control value	diabetic value
X_{F1} (F1-F0 activity)	150.93	0.0410
X_{C1} (complex I activity)	0.36923	0.1063
X_{HLE} (proton leak activity)	250	437.8554

of control cellular ultrastructure with control mitochondrial metabolism (Set CC, 19 simulations).

Mitochondrial dysfunction in the step CD and DD were simulated by modifying the values of four key parameters present in the mitochondrial model. These parameters are: (i) complex I enzyme activity (X_{C1}); (ii) F1-F0 enzyme activity (X_{F1}); (iii) proton leak activity (X_{HLE}); and (iv) maximal mtCK reaction rates in forward and backward direction (V_1 and V_{-1}). For example, several experimental studies indicate that mtCK enzyme activity (IU mg^{-1} myocardial protein) can be decreased by a margin of 35%–50% in cardiomyocytes after eight weeks of STZ-induced diabetes [9,27,40]. Based on these studies, both V_1 and V_{-1} were decreased by a margin of 50% to simulate the diabetic mtCK reactions. Similarly, Pham *et al.* [5] reported a 35% decrease in mitochondrial ATP synthesis rate, 24% decrease in O$_2$ consumption rate and unchanged membrane potential during state III respiration in cardiac tissue homogenates from eight-week STZ-induced T1D SD rat hearts. These changes were reproduced in the model by finding values of X_{C1}, X_{F1} and X_{HLE} that lead to changes in mitochondrial ATP synthesis rate, O$_2$ consumption rate and membrane potential equivalent to that observed in diabetic tissue homogenates. Lsqnonlin, a nonlinear data fitting function in MATLAB [46] was used to estimate these parameters. Table 1 presents the control values of V_1, V_{-1}, X_{C1}, X_{F1} and X_{HLE} alongside the diabetic values of these parameters.

(e) Statistical analysis

A linear mixed model (LMM) [47] was used to test if a given variable, e.g. mitochondrial area fraction, shows any difference across the different conditions. For each LMM, the random effect indicates the multiple cross-sections obtained for each rat. The fixed effects of each model are the rat's conditions, such as control and diabetes for image analysis or CC, CD and DD for simulations results. The parameters of the LMM were estimated using the restricted maximum-likelihood procedure. The marginal contribution of each condition was tested using the *t*-statistics.

Correlation between two measurements was quantified by Pearson correlation coefficient, and *t*-statistics were employed to test if the correlation differs from the null value. The electronic supplementary material, Methods S1 provides a detailed discussion of the statistical tools used to analyse the model predictions and results from image analysis.

3. Results

(a) Type I diabetes changes area fractions and organization of intracellular organelles

The pie charts in figure 1*c* presents the organelle area fractions averaged over the three animals in both control and diabetic group. It is evident from figure 1*c* that control animals contain a higher fraction of mitochondria (43% in control versus 37% in T1D), while the diabetic animals contain a higher fraction of glycogen particles (2% in control versus 9% in T1D). The average area fraction of myofibrils did not change significantly in diabetic animals. The boxplots in the electronic supplementary material, figure S1D provides the MADs of the mito/myo$_{local}$ distributions, averaged over control and diabetic animals. The average MAD of mito/myo$_{local}$ distributions increased mildly (0.083 versus 0.094)
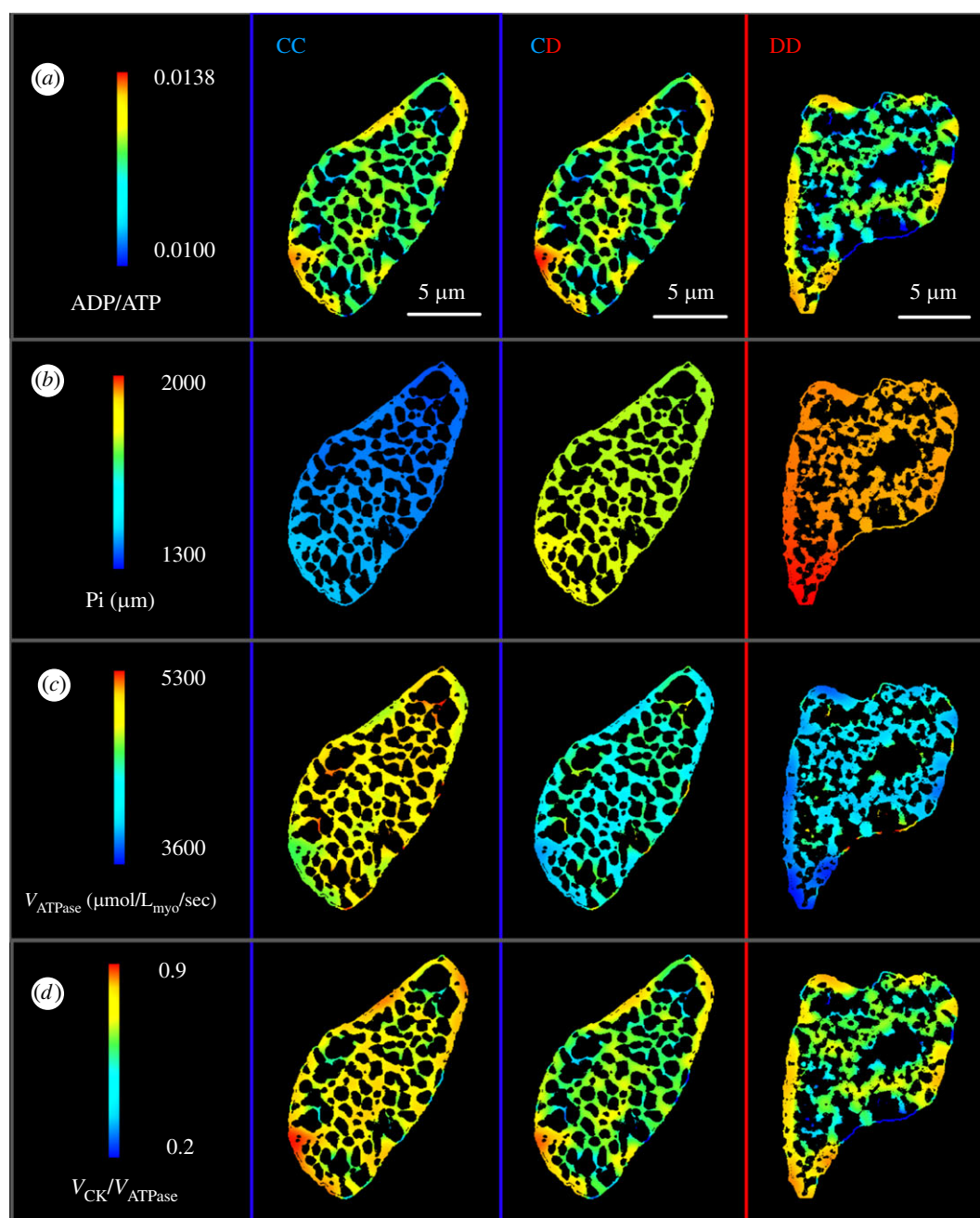
Figure 3. Model predicted spatial distributions of key metabolic parameters in the myofibrillar regions of representative control and diabetic cross-sections. Each column of the figure presents results from three distinct simulation sets—control mitochondrial metabolism with control ultrastructure (set CC—column 1), diabetic mitochondrial metabolism with control ultrastructure (set CD—column 2) and diabetic mitochondrial metabolism with diabetic ultrastructure (set DD—column 3). The regions belonging to mitochondria, glycogen and t-tubule are shown in black as part of the background. Each row of the figure represents a particular metabolic parameter: (*a*) distributions of myofibrillar ADP/ATP ratios; (*b*) distributions of myofibrillar Pi; (*c*) distributions of myofibrillar V_{ATPase}; and (*d*) distributions of myofibrillar V_{CK}/V_{ATPase} ratio.

in the diabetic group. The higher MAD implies that arrangement of mitochondria and myofibrils is more non-uniform in diabetic cross-sections compared to control cross-sections.

(b) Myofibrillar ATP metabolism is altered in type I diabetes

Figure 3 presents colour spectrum maps of a few key bioenergetic parameters which regulate cross-bridge cycling in myofibrils. These include results from three different simulations (CC, CD and DD) based on the two representative cross-sections previously shown in figure 1*a,b*. The same high value of X_{ATPase} ($X_{ATPase} = 0.01$), indicating a high Ca^{2+}-induced activity of the actomyosin complexes, was used as a model input for the three simulations. This helped in evaluating cardiac bioenergetics independent of alterations in Ca^{2+} dynamics.

The ratio of ADP and ATP concentration is considered as a key regulator of sarcomere shortening velocity and force development [48,49]. We can observe in figure 3*a* that myofibril areas located away from mitochondria have a higher ADP/ATP ratio compared to the cell wide average. Compared to simulation CC, this effect is more prominent in simulation CD and DD. We further observe variation in the myofibrillar concentration of Pi in all simulations (figure 3*b*). However, gradients of Pi concentration appear to be weaker than ADP/ATP gradients. Myofibrillar ADP/ATP ratio can change drastically within 1 μm, depending
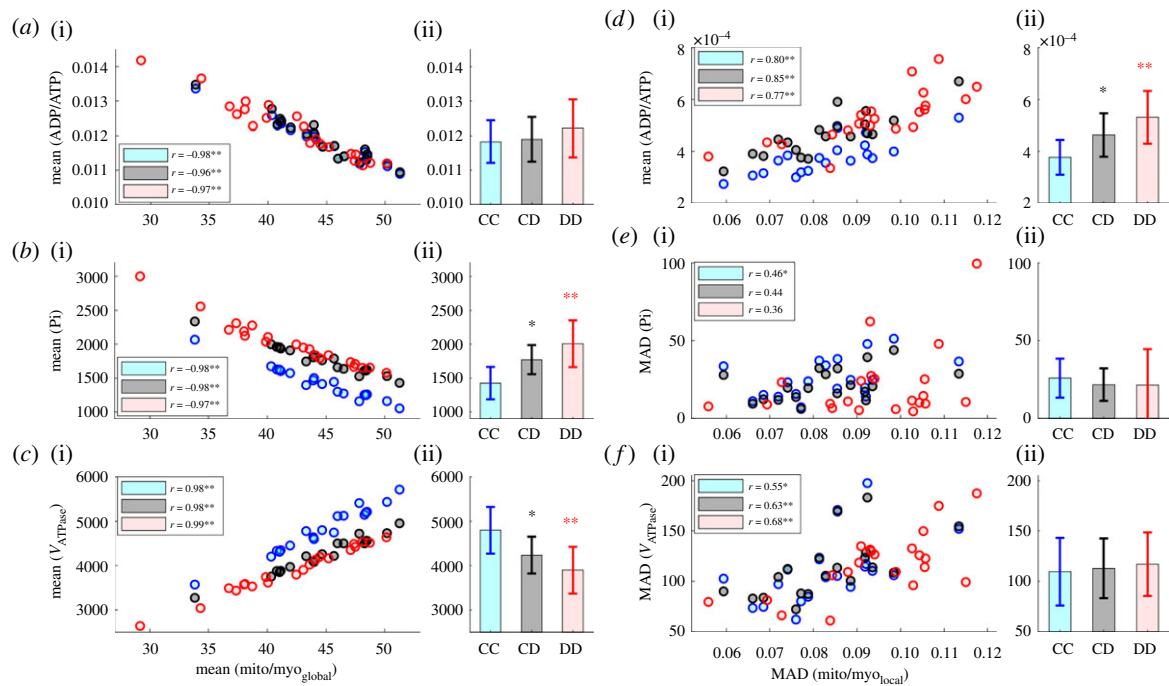
Figure 4. Relationship between cardiac ultrastructure and energy metabolism. The scatterplots show the spatial average and MAD of metabolic parameters in each cross-section as a function of either corresponding average mito/myo$_{global}$ ratio or MAD of mito/myo$_{local}$ ratio. Each scatter plot contains results from simulation set CC (19 control cross-sections), CD (19 control cross-sections) and DD (21 diabetic cross-sections). The legends show the Pearson correlation coefficient (r) separately for each simulation set. The p-value corresponding to the null hypothesis of no correlation is indicated as either *(0.05 ≥ p > 0.01) or **(0.01 ≥ p). The bar plots located next to the scatterplots show the spatially averaged ADP/ATP ratios further averaged over three animals corresponding to each simulation set. The p-values indicated as *(0.05 ≥ p > 0.01) or **(0.01 ≥ p) correspond to the null hypothesis of unchanged value from CC. (*a*) (i) ADP/ATP ratios in each cross-section and (ii) their simulation averages. (*b*) (i) Average Pi concentration (μM) in each cross-section and (ii) their simulation averages. (*c*) (i) Average V_{ATPase} (μmol l^{-1}. myofibrils s^{-1} in each cross-section and (ii) their simulation averages. (*d*) (i) MAD of ADP/ATP ratios in each cross-section and (ii) their simulation averages. (*e*) (i) MAD of Pi concentration in each cross-section and (ii) their simulation averages. (*f*) (i) MAD of V_{ATPase} in each cross-section and (ii) their simulation averages.

on proximity to mitochondria. By contrast, Pi concentration does not exhibit strong localized gradients and rather changes gradually from one end of a cross-section to the other. The simulations also predict a large difference in spatially averaged Pi concentrations in the three simulations. Average Pi is lowest in the simulation CC, and it cumulatively increases as mitochondrial dysfunction and diabetic ultrastructure are introduced in simulations CD and DD.

Figure 3c shows the profiles of myofibrillar V_{ATPase} in the three simulations. The average V_{ATPase} is highest in the control simulation, and it declines with the introduction of both mitochondrial dysfunction and diabetic ultrastructure. The model parameters influencing these results and their statistical significance has been discussed in detail in the next sub-section (figure 4). Owing to our steady state assumptions, total ATP hydrolysis in the myofibrils (V_{ATPase} × Area$_{myofibrils}$) balances mitochondrial ATP synthesis (V_{F1-F0} × Area$_{mitochondria}$) in all the three simulations. This is evident in the electronic supplementary material, figure S3A, where average V_{F1-F0} drops to a lower level with introduction of mitochondrial dysfunction in simulation CD. While the average V_{F1-F0} appears to be same between simulation CD and DD, the total ATP synthesis is further diminished in DD owing to a lower mitochondrial area fraction.

(c) Type I diabetes alters the phosphocreatine shuttle

Owing to cytosolic diffusion barriers, ATP produced in the mitochondria diffuses slowly towards the myofibrils [50]. This diffusion rate (diffusivity = 30 μm s^{-1}) is usually not

sufficient to fulfil the demand of ATP during a high cross-bridge workload. However, myofibrillar CK enzyme can locally regenerate ATP by transferring the phosphate group of PCr to ADP (ADP + PCr ⇌ ATP + Cr). The generated Cr rapidly diffuses (diffusivity = 260 μm s^{-1}) to the mitochondrial IMS, where mtCK converts it back to PCr (ADP + PCr ⇌ ATP + Cr) through the reverse reaction (figure 2). The PCr synthesized by mitochondrial CK diffuses back to the myofibrils, thus completing a circular reaction pathway. This CK-mediated pathway of ADP/ATP exchange is also known as the PCr shuttle. The ratio between reaction rates of myofibrillar CK enzyme and ATP hydrolysis (V_{CK}/V_{ATPase}) indicates the fraction of ATP used by the cross-bridge cycle that is exchanged through this pathway.

Figure 3d reveals that myofibril units adjacent to mitochondria have a lower V_{CK}/V_{ATPase} compared to myofibrils located away from the mitochondrial columns. This trend is noticeable in all the three simulations. The results signify that a higher fraction of ATP is regenerated through myofibrillar CK, when diffusion distance between mitochondria and myofibrils is longer. On the other hand, the direct exchange of ATP and ADP through diffusion takes a shorter time when myofibrils are in the vicinity of mitochondria. Therefore, less ADP is available to drive the myofibrillar CK enzymatic reactions forward.

In all steady state simulations, total PCr synthesis in the mitochondria (V_{mtCK} × Area$_{myofibrils}$) is balanced by the total PCr consumption (V_{CK} × Area$_{mitochondria}$) in myofibrils. In simulations CD and DD, the activity of mtCK is decreased by half. Consequently, CK reaction rates decline substantially

in both mitochondria and myofibrils. This result is reflected in the visibly lower average V_{CK}/V_{ATPase} in simulation CD and DD compared to CC (figure 3d). The results imply that mitochondrial dysfunction weaken the PCr shuttle and encourage more direct diffusion based exchange of ADP and ATP. In addition, lower CK reaction rate leads to a large decline in myofibrillar PCr/ATP ratio as shown in the electronic supplementary material, figure S3B.

(d) Relationship between organelle area fractions and energy metabolism

Figure 4a(i),b(i) show the spatially averaged ADP/ATP ratios and Pi concentrations corresponding to the 19 control and 21 diabetic cross-sections. These have been plotted in conjunction with the ratio of mitochondrial area fraction against total mitochondrial and myofibrillar area fraction (mito/myo$_{global}$) of each section. Averages of both ADP/ATP ratio and Pi concentration show a strong negative correlation with the mito/myo$_{global}$ ratios. Since V_{ATPase} is modelled as an inverse function of ADP/ATP ratio and Pi concentration, average V_{ATPase} correlates positively with the mito/myo$_{global}$ ratio of each cell cross-section (figure 4c(i)). The boxplots in figure 4a(ii) reveal the absence of any significant change in spatially averaged ADP/ATP ratios with the introduction of mitochondrial dysfunction (CD) and structural changes (DD). By contrast, Pi concentration is lowest in simulation set CC (figure 4b(ii)), and it successively rises in CD (24%) and DD (40%). We also observe a reverse trend with V_{ATPase} in figure 4c(ii).

(e) Relationship between heterogeneity in ultrastructure and energy metabolism

MADs of the spatial distribution of myofibrillar ADP/ATP ratio, Pi concentration and V_{ATPase} act as indicators of the heterogeneity of the metabolic landscape in a cell cross-section. Similarly, the MAD of mito/myo$_{local}$ distribution provides an indirect estimate of the structural heterogeneity within a given cross-section. As evident from the scatterplot in figure 4d(i), MAD of ADP/ATP appears to increase with higher MAD of mito/myo$_{local}$ distribution in all three simulations sets. This positive correlation is evident in all three simulation sets. By contrast, no statistically significant correlation was observed between MAD of mito/myo$_{local}$ and MADs of Pi in any of the three simulation sets (figure 4e(i)).

The boxplots in the figure 4d(ii) reveal that structural alterations and mitochondrial dysfunction in simulation set DD lead to a 41% higher average MAD of ADP/ATP distribution compared to set CC. When results between simulation set CC and CD are compared, we can also observe a 23% rise in MAD of ADP/ATP ratio owing to the introduction of mitochondrial dysfunction independent of structural alterations. The results suggest that when ATP demand is high, diabetic cell cross-sections will have stronger concentration gradients of ADP and ATP compared to their control counterparts. Unlike ADP/ATP ratio, the MADs of Pi concentration and V_{ATPase} exhibited no statistically significant difference between results from the three simulation sets. These results are consistent with the weak Pi concertation gradients previously observed in figure 3b.

4. Discussion

(a) Effects of diabetic mitochondrial dysfunction on cardiac energy metabolism

In simulation CD, the model of mitochondrial metabolism incorporates lower enzymatic activity of complex I and F1-F0 ATP synthase along with elevated proton leak activity (table 1). All of these changes diminish the capacity of mitochondria to synthesize ATP, which ultimately leads to a 12% decrease in both mitochondrial V_{F1-F0} and myofibrillar V_{ATPase}. In myofibrils, the lower V_{ATPase} is driven by a 24% higher concentration of Pi. However, the average myofibrillar ADP/ATP remains at nearly the same level. This result can be explained by the well-established role of PCr as a buffer of ATP [51,52]. The myofibrillar CK enzymes convert the excess build-up of ADP to ATP at the cost of the depleted PCr reserve (electronic supplementary material, figure S3B). A substantial part of the ADP produced from ATP hydrolysis is also relocated to the mitochondrial matrix, where it helps to drive the ATP synthesis forward despite the lower F1-F0 activity.

Another important prediction of our model is decrease in CK-mediated ADP/ATP exchange in T1D cardiomyopathy. Phospho-transfer between cardiac mitochondria and myofibrils occurs through three competitive pathways (electronic supplementary material, figure S3). These include direct diffusion of ADP and ATP, alongside CK-mediated PCr shuttle. According to an experimental study by Dzeja et al. on isolated mice hearts [53], PCr shuttle accounts for 69% of the total ADP/ATP exchange between mitochondria and myofibrils. Our control simulations (CC) also predict the average contribution of this shuttle (V_{CK}/V_{ATPase}) to be in a similar percentage range (figure 3d). However, in simulation CD, the contribution of PCr shuttle is reduced. Consequently, the diffusion of ADP and ATP accounts for a higher proportion of total phospho-transfer in T1D cardiomyopathy.

Myofibrillar diffusivity of ADP and ATP is almost 10 times lower than that of Pi, PCr and Cr [50]. Due to the low diffusivity, ADP and ATP require stronger concentration gradients than PCr and Cr to facilitate the same amount of phospho-transfer. As a result, myofibril areas with higher mito/myo$_{local}$ density appear to have lower ADP/ATP, while myofibrils not in vicinity of mitochondria have high ADP/ATP ratio (figure 3a). This also explains why ADP/ATP ratio exhibits heterogeneous spatial distribution unlike that of Pi (figure 3b). When it comes to simulation CD, the concentration gradients of ADP and ATP need to be even sharper to ensure their higher share of total phospho-transfer. Consequently, ADP/ATP distribution is significantly more heterogenous in simulation CD compared to CC (figure 4d).

(b) Ultrastructural alterations and their effect on cardiac energy metabolism

The analysis of TEM images in figure 1c reveals that diabetic cardiomyocyte cross-sections have a significantly lower area fraction of mitochondria (37%) compared to their control counterparts (43%). At the same time, the area fraction of myofibrils does not change significantly, implying a lower ATP synthesis capacity per unit area of myofibrils in diabetic

cardiomyocytes. These results are in close agreement with a previous imaging study by Searls *et al.* [24] on STZ-induced T1D SD rat cardiomyocytes. Searls *et al.* found a significant reduction in mitochondrial area fraction (44.5% in control versus 36% in T1D) without any significant change in myofibrillar area fraction. Similar results have been also reported by Li *et al.* [25].

As evident from the model predictions in figure 4*c*, the lower availability of mitochondria in diabetic cross-sections decreases the average V_{ATPase} in myofibrils (simulation DD). However, the average ADP/ATP ratio remains unchanged owing to buffering by myofibrillar PCr. Previously, based on data from T1D OVE26 mice, Shen *et al.* [14] proposed higher mitochondrial fraction as a compensatory response to mitochondrial dysfunction in T1D cardiomyopathy. Our model predictions contrast with this hypothesis and instead suggests lower mitochondrial area fraction as a mechanism that further exacerbates the negative impact of impaired OXPHOS (simulation DD versus CD).

Besides lower mitochondrial fraction, the arrangement of mitochondria and myofibrils is more non-uniform in T1D cardiomyopathy. This result is evident from the higher MAD of mito/myo$_{local}$ ratio in the diabetic cross-sections (electronic supplementary material, figure S1D). The increased spatial heterogeneity of mito/myo$_{local}$ ratio is also reflected in the higher MAD of ADP/ATP ratio in simulation DD (figure 4*d*). In simulation CD, MAD of ADP/ATP ratio increases owing to elevation in diffusive fluxes of ADP and ATP. The non-uniform arrangement of mitochondria and myofibrils further contributes to this heterogenous metabolic landscape in simulation DD. The observed spatial variation in ADP/ATP might lead to variation in actomyosin contraction velocity between different parts of a cell [48,49]. This may result in intracellular shear strain, along with negative consequences for the cellular ultrastructure. This model-informed hypothesis will require new precision experimental measurements.

5. Limitations and further work

A logical next step of the current work will be to couple our model of cardiac bioenergetics with models of Ca^{2+} signalling and cross-bridge cycling [48,49]. This will enable us to translate the predictions of altered ADP/ATP level and Pi concentration in T1D cardiomyopathy to corresponding changes in cardiac force dynamics and contractility. More-over, many previous studies report elevated intrinsic stiffness of cardiomyocytes owing to diabetes [54,55]. A coupled bioenergetics-mechanics model of cardiomyocytes will be a useful tool to investigate the overall effects of the alterations in metabolism, ultrastructure and material properties. There is also scope to improve the current model of cardiac bioenergetics by incorporating details of glycolysis, beta oxidation and subsequent tricarboxylic acid (TCA) cycle.

On the image analysis side, a more complete analysis of the three-dimensional organization of mitochondrial columns and other organelles between control and T1D is needed. According to a recent work by Glancy *et al.* [10], cardiac mito-chondria form a series of interconnected networks which can conduct electricity similar to power grids. These networks can dynamically respond to stress by electrically separating malfunctioning mitochondria. Another previous study

indicates that the extent of T1D-induced ultrastructural alterations can vary between different mitochondrial sub-populations within the same cell [19].

Regardless of the limitations discussed above, the EM image analysis in this study provides many new insights on cardiac ultrastructure that were not reported previously, e.g. more non-uniform distribution of mitochondria and myofibrils in T1D cardiomyopathy. The current study is also, to our knowledge, the first attempt in literature to create a spatially detailed mathematical model of cardiac energy metabolism in T1D cardiomyopathy. The model provides a simplistic representation of the diminished ATP and PCr synthesis capacity of diabetic mitochondria, which we used to understand the relationship between cardiac ultrastructure and bioenergetics.

6. Conclusion

Alterations in the columnar ultrastructure of cardiac mitochondria is observed in several cardiac disease con-ditions. The primary aim of the current study was to understand the functional role of these ultrastructural altera-tions in the context of STZ-induced T1D cardiomyopathy as a model disease state. Our bioenergetics simulations predict that diabetic cardiomyocytes have a higher level of myo-fibrillar Pi and lower ATP hydrolysis rate compared to control cardiomyocytes, in response to the same level of cross-bridge cycle stimulation. These results are a conse-quence of lower availability of mitochondria per unit area of myofibrils, as well as impaired OXPHOS capacity of indi-vidual mitochondrion. Our simulations further reveal that spatial average of myofibrillar ADP/ATP ratio is not affected in T1D cardiomyopathy. However, the spatial distribution of ADP/ATP ratio becomes more heterogeneous in diabetic cross-sections owing to a more irregular arrangement of mitochondria and myofibrils and an increased dependence of the cell on direct ATP-ADP diffusion to meet the ATP demands of myofibrils. Overall, our study indicates that alterations in cardiac ultrastructure such as lower mitochon-drial area fraction and irregular mitochondrial–myofibrillar arrangement further aggravate the metabolic disruptions preceding the ultrastructural alterations. Future work will include using a coupled bioenergetics-mechanics model to assess the impact of the observed metabolic disruptions on the cardiac force dynamics and contractility.

Authors' contributions. S.G.: conceptualization, formal analysis, investi-gation, methodology, validation, visualization, writing—original draft, writing—review and editing; G.G.: formal analysis, method-ology, writing—original draft, writing—review and editing; I.O.: conceptualization, data curation, methodology, writing—review and editing; F.S.: resources, supervision, writing—review and editing; A..H.: methodology, writing—review and editing; E.H.: method-ology, writing—review and editing; V.R.: conceptualization, project

References

1. American Diabetes Association. 2009 Diagnosis and classification of diabetes mellitus. *Diabet. Care* **32**(Suppl. 1), S62–S67.

2. Maahs DM, West NA, Lawrence JM, Mayer-Davis EJ. 2010 Epidemiology of type 1 diabetes. *Endocrinol. Metab. Clin. North Am.* **39**, 481–497. (doi:10.1016/j.ecl.2010.05.011)

3. Miki T, Yuda S, Kouzu H, Miura TJH. 2013 Diabetic cardiomyopathy: pathophysiology and clinical features. *Heart Fail Rev.* **18**, 149–166.

4. Huynh K, Bernardo BC, McMullen JR, Ritchie RH. 2014 Diabetic cardiomyopathy: mechanisms and new treatment strategies targeting antioxidant signaling pathways. *Pharmacol. Ther.* **142**, 375–415. (doi:10.1016/j.pharmthera.2014.01.003)

5. Pham T, Loiselle D, Power A, Hickey AJR. 2014 Mitochondrial inefficiencies and anoxic ATP hydrolysis capacities in diabetic rat heart. *Am. J. Physiol.* **307**, C499-C507. (doi:10.1152/ajpcell.00006.2014)

6. Bugger H *et al.* 2008 Type 1 diabetic akita mouse hearts are insulin sensitive but manifest structurally abnormal mitochondria that remain coupled despite increased uncoupling protein 3. *Diabetes* **57**, 2924–2932. (doi:10.2337/db08-0079)

7. Lashin OM, Szweda PA, Szweda LI, Romani AMP. 2006 Decreased complex II respiration and HNE-modified SDH subunit in diabetic heart. *Free Radical Biol. Med.* **40**, 886–896. (doi:10.1016/j.freeradbiomed.2005.10.040)

8. Jilkina O, Kuzio B, Kupriyanov VV. 2008 Potassium fluxes, energy metabolism, and oxygenation in intact diabetic rat hearts under normal and stress conditions. *Can. J. Physiol. Pharmacol.* **86**, 710–725. (doi:10.1139/Y08-076)

9. Savabi F, Kirsch A. 1991 Alteration of the phosphocreatine energy shuttle components in diabetic rat heart. *J. Mol. Cell. Cardiol.* **23**, 1323–1333. (doi:10.1016/0022-2828(91)90089-5)

10. Glancy B, Hartnell LM, Combs CA, Fenmou A, Sun J, Murphy E, Subramaniam S, Balaban RS. 2017 Power grid protection of the muscle mitochondrial reticulum. *Cell Rep.* **19**, 487–496. (doi:10.1016/j.celrep.2017.03.063)

11. Bleck CK, Kim Y, Willingham TB, Glancy BJN. 2018 Subcellular connectomic analyses of energy networks in striated muscle. *Nat. Commun.* **9**, 1–11.

12. Picard M *et al.* 2015 Trans-mitochondrial coordination of cristae at regulated membrane junctions. *Nat. Commun.* **6**, 1–8.

13. Huang X *et al.* 2013 Kissing and nanotunneling mediate intermitochondrial communication in the heart. *Proc. Natl Acad. Sci. USA* **110**, 2846–2851. (doi:10.1073/pnas.1300741110)

14. Shen X, Zheng S, Metreveli NS, Epstein PN. 2006 Protection of cardiac mitochondria by overexpression of MnSOD reduces diabetic cardiomyopathy. *Diabetes* **55**, 798–805. (doi:10.2337/diabetes.55.03.06.db05-1039)

15. Fitzl G, Welt K, Wassilew G, Clemens N, Penka K, Mükke N. 2001 The influence of hypoxia on the myocardium of experimentally diabetic rats with and without protection by Ginkgo biloba extract: III: ultrastructural investigations on mitochondria. *Exp. Toxicol. Pathol.* **52**, 557–568. (doi:10.1016/S0940-2993(01)80017-8)

16. Ong S-B, Subrayan S, Lim SY, Yellon DM, Davidson SM, Hausenloy DJ. 2010 Inhibiting mitochondrial fission protects the heart against ischemia/reperfusion injury. *Circulation* **121**, 2012–2222. (doi:10.1161/CIRCULATIONAHA.109.906610)

17. Sudarikova YV, Bakeeva LE, Tsiplenkova VG. 1997 Ultrastructure of mitochondrial reticulum of human cardiomyocytes in alcohol cardiomyopathy. *Biochem. Biokhimiia* **62**, 989–1002.

18. Plotnikov EY, Vasileva AK, Arkhangelskaya AA, Pevzner IB, Skulachev VP, Zorov DB. 2008 Interrelations of mitochondrial fragmentation and cell death under ischemia/reoxygenation and UV-irradiation: protective effects of SkQ1, lithium ions and insulin. *FEBS Lett.* **582**, 3117–3124. (doi:10.1016/j.febslet.2008.08.002)

19. Williamson CL, Dabkowski ER, Baseler WA, Croston TL, Alway SE, Hollander JM. 2010 Enhanced apoptotic propensity in diabetic cardiac mitochondria: influence of subcellular spatial location. *Am. J. Physiol. Heart Circ. Physiol.* **298**, H633-H642. (doi:10.1152/ajpheart.00668.2009)

20. Galloway CA, Yoon Y. 2013 Mitochondrial morphology in metabolic diseases. *Antioxid. Redox Signal.* **19**, 415–430. (doi:10.1089/ars.2012.4779)

21. Jarosz J, Ghosh S, Delbridge LMD, Petzer A, Hickey AJR, Crampin EJ, Hanssen E, Rajagopal V. 2017 Changes in mitochondrial morphology and organization can enhance energy supply from mitochondrial oxidative phosphorylation in diabetic cardiomyopathy. *Am. J. Physiol.* **312**, C190-C197. (doi:10.1152/ajpcell.00298.2016)

22. Shen X, Zheng S, Thongboonkerd V, Xu M, Pierce WM, Klein JB, Epstein PN. 2004 Cardiac mitochondrial damage and biogenesis in a chronic model of type 1 diabetes. *Am. J. Physiol. Endocrinol. Metabolism* **287**, E896-E905. (doi:10.1152/ajpendo.00047.2004)

23. Vazquez EJ, Berthiaume JM, Kamath V, Achike O, Buchanan E, Montano MM, Chandler MP, Miyagi M, Rosca MG. 2015 Mitochondrial complex I defect and increased fatty acid oxidation enhance protein lysine acetylation in the diabetic heart. *Cardiovasc. Res.* **107**, 453–465. (doi:10.1093/cvr/cvv183)

24. Searls YM, Smirnova IV, Fegley BR, Stehno-Bittel L. 2004 Exercise attenuates diabetes-induced ultrastructural changes in rat cardiac tissue. *Med. Sci. Sports Exerc.* **36**, 1863–1870. (doi:10.1249/01.MSS.0000145461.38224.EC)

25. Li Y-G, Dong Z, Chen K, He Y, Dai X, Li S, Li J, Zhu W, Wei M. 2017 Insulin upregulates GRIM-19 and protects cardiac mitochondrial morphology in type 1 diabetic rats partly through PI3 K/AKT signaling pathway. *Biochem. Biophys. Res. Commun.* **493**, 611–617. (doi:10.1016/j.bbrc.2017.08.144)

26. Thompson EW. 1988 Structural manifestations of diabetic cardiomyopathy in the rat and its reversal by insulin treatment. *Am. J. Anatomy* **182**, 270–282. (doi:10.1002/aja.1001820308)

27. Spindler M, Saupe KW, Tian R, Ahmed S, Matlib MA, Ingwall JS. 1999 Altered creatine kinase enzyme kinetics in diabetic cardiomyopathy. A31P NMR magnetization transfer study of the intact beating rat heart. *J. Mol. Cell. Cardiol.* **31**, 2175–2189. (doi:10.1006/jmcc.1999.1044)

28. Boudina S, Sena S, O'Neill BT, Tathireddy P, Young ME, Abel ED. 2005 Reduced mitochondrial oxidative capacity and increased mitochondrial uncoupling impair myocardial energetics in obesity. *Circulation* **112**, 2686–2695. (doi:10.1161/CIRCULATIONAHA.105.554360)

29. Duncan JG, Fong JL, Medeiros DM, Finck BN, Kelly DP. 2007 Insulin-resistant heart exhibits a mitochondrial biogenic response driven by the peroxisome proliferator-activated receptor gene regulatory pathway. *Circulation* **115**, 909–917. (doi:10.1161/CIRCULATIONAHA.106.662296)

30. Ghosh S *et al.* 2018 Insights on the impact of mitochondrial organisation on bioenergetics in high-resolution computational models of cardiac cell architecture. *PLoS Comput. Biol.* **14**, e1006640. (doi:10.1371/journal.pcbi.1006640)

31. Ghosh S. 2019 Role of ultrastructural alterations in diabetic cardiomyopathy. PhD thesis, University of Melbourne, Melbourne, Australia.

32. Hussain A, Ghosh S, Kalkhoran SB, Hausenloy DJ, Hanssen E, Rajagopal V. 2018 An automated workflow for segmenting single adult cardiac cells from large-volume serial block-face scanning electron microscopy data. *J. Struct. Biol.* **202**, 275–285. (doi:10.1016/j.jsb.2018.02.005)

33. Yan J *et al.* 2012 Visualization, modeling, and spatial statistics of mitochondrial assembly in adult cardiomyocytes using serial block-face scanning electron microscopy. *J. Struct. Biol.* **102**, 142a.

34. Arganda-Carreras I *et al*. 2017 Trainable Weka segmentation: a machine learning tool for microscopy pixel classification. *Bioinformatics* **33**, 2424–2426.

35. Shewchuk JR (ed). 1996 *Triangle: engineering a 2D quality mesh generator and delaunay triangulator. Workshop on applied computational geometry.* Berlin, Germany: Springer.

36. Beard DA. 2005 A biophysical model of the mitochondrial respiratory system and oxidative phosphorylation. *PLoS Comput. Biol.* **1**, e36. (doi:10.1371/journal.pcbi.0010036)

37. Bradley C *et al*. 2011 OpenCMISS: a multi-physics & multi-scale computational infrastructure for the VPH/Physiome project. **107**, 32–47.

38. Baseler WA, Thapa D, Jagannathan R, Dabkowski ER, Croston TL, Hollander JM. 2012 miR-141 as a regulator of the mitochondrial phosphate carrier (Slc25a3) in the type 1 diabetic heart. *Am. J. Physiol.* **303**, C1244–C1251. (doi:10.1152/ajpcell.00137.2012)

39. Ni R *et al*. 2016 Mitochondrial calpain-1 disrupts ATP synthase and induces superoxide generation in type 1 diabetic hearts: a novel mechanism contributing to diabetic cardiomyopathy. *Diabetes* **65**, 255–268. (doi:10.2337/db15-0963)

40. Veksler VI, Murat I, Ventura-Clapier R. 1991 Creatine kinase and mechanical and mitochondrial functions in hereditary and diabetic cardiomyopathies. *Can. J. Physiol. Pharmacol.* **69**, 852–858. (doi:10.1139/y91-129)

41. Huynh K, Kiriazis H, Du X-J, Love JE, Gray SP, Jandeleit-Dahm KA, Mcmullen JR, Ritchie RH. 2013 Targeting the upregulation of reactive oxygen species subsequent to hyperglycemia prevents type 1 diabetic cardiomyopathy in mice. *Free Radical Biol. Med.* **60**, 307–317. (doi:10.1016/j.freeradbiomed.2013.02.021)

42. Herlein JA, Fink BD, O'Malley Y, Sivitz WI. 2009 Superoxide and respiratory coupling in mitochondria of insulin-deficient diabetic rats. *Endocrinology* **150**, 46–55. (doi:10.1210/en.2008-0404)

43. Dabkowski ER, Williamson CL, Bukowski VC, Chapman RS, Leonard SS, Peer CJ, Callery PS, Hollander JM. 2009 Diabetic cardiomyopathy-associated dysfunction in spatially distinct mitochondrial subpopulations. *Am. J. Physiol.* **296**, H359–H369. (doi:10.1152/ajpheart.00467.2008)

44. Tanaka Y, Konno N, Kako KJ. 1992 Mitochondrial dysfunction observed *in situ* in cardiomyocytes of rats in experimental diabetes. *Cardiovasc. Res.* **26**, 409–414. (doi:10.1093/cvr/26.4.409)

45. Ziegelhoffer A *et al*. 2009 Calcium signaling-mediated endogenous protection of cell energetics in the acutely diabetic myocardium. *Can. J. Physiol. Pharmacol.* **87**, 1083–1094. (doi:10.1139/Y09-108)

46. The MathWorks Inc. 2016 MATLAB and Image Processing Toolbox 2016a, Natick, Massachusetts, United States.

47. Tuerlinckx F, Rijmen F, Verbeke G, De Boeck PJBJoM, Psychology S. 2006 Statistical inference in generalized linear mixed models: a review. **59**, 225–255.

48. Tran K, Smith NP, Loiselle DS, Crampin EJ. 2010 A metabolite-sensitive, thermodynamically constrained model of cardiac cross-bridge cycling: implications for force development during ischemia. *Biophys. J.* **98**, 267–276. (doi:10.1016/j.bpj.2009.10.011)

49. Tewari SG, Bugenhagen SM, Palmer BM, Beard DA. 2016 Dynamics of cross-bridge cycling, ATP hydrolysis, force generation, and deformation in cardiac muscle. *J. Mol. Cell. Cardiol.* **96**, 11–25. (doi:10.1016/j.yjmcc.2015.02.006)

50. Simson P, Jepihhina N, Laasmaa M, Peterson P, Birkedal R, Vendelin M. 2016 Restricted ADP movement in cardiomyocytes: cytosolic diffusion obstacles are complemented with a small number of open mitochondrial voltage-dependent anion channels. *J. Mol. Cell. Cardiol.* **97**, 197–203. (doi:10.1016/j.yjmcc.2016.04.012)

51. Vendelin M, Kongas O, Saks V. 2000 Regulation of mitochondrial respiration in heart cells analyzed by reaction-diffusion model of energy transfer. *Am. J. Physiol.* **278**, C747–C764. (doi:10.1152/ajpcell.2000.278.4.C747)

52. Meyer RA, Sweeney HL, Kushmerick MJ. 1984 A simple analysis of the 'phosphocreatine shuttle'. *Am. J. Physiol.* **246**, C365–C377. (doi:10.1152/ajpcell.1984.246.5.C365)

53. Dzeja PP, Hoyer K, Tian R, Zhang S, Nemutlu E, Spindler M, Ingwall JS. 2011 Rearrangement of energetic and substrate utilization networks compensate for chronic myocardial creatine kinase deficiency. *J. Physiol.* **589**, 5193–5211. (doi:10.1113/jphysiol.2011.212829)

54. Benech JC *et al*. 2014 Diabetes increases stiffness of live cardiomyocytes measured by atomic force microscopy nanoindentation. *Am. J. Physiol. Cell Physiol.* **307**, C910–C919.

55. Nikolajević SJ, Janić M. 2019 Molecular mechanisms responsible for diastolic dysfunction in diabetes mellitus patients. *Int. J. Mol. Sci.* **20**, 1197.

56. Ghosh S, Guglielmi G, Orfanidis I, Spill F, Hickey A, Hanssen E, Rajagopal V. 2022 Effects of altered cellular ultrastructure on energy metabolism in diabetic cardiomyopathy: an *in silico* study. FigShare. (doi:10.6084/m9.figshare.c.6135969)